DFT Study of $TlSrF_3$: Structural, Optical, and Thermodynamic Properties

H. Mesbah[a,*], M.N. Belkaid[a], M. Kadjaoud[b], M.I. Ziane[c], Y. Larbah[d] and T. Khatir[e]

[a] *Laboratory of Radiation Analysis and Applications (LAAR), University of Science and Technology Oran, Mohamed Boudiaf, PO Box 1505, El M'Naouar, 31000 Oran, Algeria*
[b] *Physics Department, Djillali Liabés University, BP 89 22000 Sidi-Bel-Abbès, Algeria*
[c] *Laboratory of Electrical and Materials Engineering (LGEM), Higher School of Electrical and Energetic Engineering of Oran (ESGEEO), Oran, Algeria*
[d] *Nuclear Research Center of Algiers (CRNA),02, Boulevard Frantz Fanon, B.P. 399, Algiers, 16000, Algeria*
[e] *Physics Department, Faculty of Science, Sétif-1 University, 19000, Setif, Algeria*

Received: 12.08.2025 & Accepted: 06.03.2026

Doi: 10.12693/APhysPolA.149.106 *e-mail: mesbahhassen7@gmail.com

Perovskite materials with the general formula ABX_3 have attracted considerable interest due to their broad potential in applications such as optoelectronics, solar energy conversion, and catalysis. In this study, the fluoroperovskite compound $TlSrF_3$ is theoretically investigated for its suitability for scintillation detector applications. A comprehensive analysis of its structural, electronic, optical, and thermodynamic properties was conducted using density functional theory. The results reveal that $TlSrF_3$ confirms a stable cubic perovskite phase with the space group $Pm\text{-}3m$ (no. 221). The calculated electronic band structure and density of states reveal a direct, wide band gap of approximately 4.40 eV at a high-symmetry point in the Brillouin zone, indicative of strong insulating behavior. Optical properties analyzed over the photon energy range of 0–14 eV show high isotropy between the ε_{xx} and ε_{zz} components, significant ultraviolet absorption, and excellent transparency in the visible region — key features for scintillation detection. Thermodynamic stability across wide temperature and pressure ranges is confirmed via the GIBBS2 code calculations. In the absence of experimental data, these theoretical insights offer a reliable foundation for future experimental validation and device-level integration. This work confirms the potential of fluoroperovskites as functional materials in advanced detection and energy technologies.

topics: fluoroperovskite $TlSrF_3$, *ab initio* calculation, optical properties, thermodynamic quantities

1. Introduction

Materials with enhanced properties are essential for advanced technological applications in a wide range of current and emerging devices [1, 2]. Perovskite materials, in particular, represent a dynamic research frontier with significant potential to revolutionize energy conversion, electronics, and advanced functional materials [3]. The perovskite structure is one of the most extensively studied frameworks in materials science [4] owing to its diverse properties, including ferroelectricity, piezoelectricity, and nonlinear optical behavior [5]. Moreover, these materials have emerged as promising candidates for spintronics [1, 2]. Based on the constituent atomic species, perovskites can be classified into three main categories: inorganic [6, 7], organic [8], and inorganic–organic hybrids [9].

The general chemical formula of perovskite compounds is ABX_3, where A and B are two cations of differing sizes, and X is an anion that is bonded to both cations [4, 10]. When fluorine atoms occupy the X site, the resulting compound is referred to as fluoroperovskite (ABF_3) [11, 12], which is well known for its distinctive geometric and physical features, such as photoluminescence and favorable optical characteristics [13]. This compound exhibits high chemical stability, wide band gaps, and excellent optical transparency, rendering it highly attractive for nonlinear optics, ultraviolet-transparent applications, and radiation detection [10, 14, 15].

Recent theoretical studies have examined Tl-based fluoroperovskites, providing insights into the properties of $TlSrF_3$. Sohail et al. [16] investigated $TlCaF_3$ and $TlCdF_3$, reporting lattice constants close to 4.19 Å, cubic structural stability, and direct band gaps of $\sim$ 5.6–5.7 eV, along

with notable optical absorption in the ultraviolet (UV) region. Khan et al. [17] investigated $TlXF_3$ (X = Zn, Sr), finding that $TlSrF_3$ possesses a direct wide band gap of approximately 4.37 eV, along with a strong dielectric response and UV optical activity. More recently, Ayub et al. [18] confirmed the dynamic (phonon) stability of $TlSrF_3$ (and $TlBeF_3$) via positive phonon dispersion relations, with an optimized lattice constant equal to $\sim$ 4.89 Å, which confirms the the robustness of its cubic structure. These cumulative findings justify the need for a deeper computational study of the electronic, optical, and structural properties of $TlSrF_3$ under varied conditions.

Despite these advances, most existing studies have either focused on structural and optical properties under standard conditions or lacked a unified evaluation of the thermodynamic behavior, electronic transitions, and energy-loss mechanisms. In addition, the scintillation potential of $TlSrF_3$ remains largely unexplored from a comprehensive theoretical perspective. These gaps underscore the need for a more integrated study to assess the full functional suitability of this material.

Interest in perovskite materials was revitalized following the discovery of high-temperature superconductors (HTSCs). These materials, in particular, have shown strong promise in direct-conversion radiation detectors due to their efficiency in converting ionizing radiation into electrical signals [10, 19, 20]. $TlSrF_3$ is a notable example within this family, adopting a cubic ABF_3-type structure, where thallium (Tl^+) and strontium (Sr^{2+}) occupy the A and B lattice sites, respectively, with the space group P$m-3m$ [21].

This study focuses on exploring the structural, electronic, optical, and thermodynamic characteristics of $TlSrF_3$ through first-principles calculations within the framework of density functional theory (DFT). Structural analysis and charge density mapping are conducted to gain insight into the bonding behavior of the compound. Furthermore, key optical parameters — including absorption coefficient, refractive index, dielectric function, and energy loss function — are systematically examined, along with thermodynamic indicators, to evaluate the suitability of $TlSrF_3$ for applications in ionizing radiation detection.

This paper is structured as follows. Section 2 outlines the computational methodology and theoretical framework. Section 3 presents and discusses the obtained results, and Sect. 4 provides the conclusions of the study.

2. Computational details

We have carried out first-principles calculations using the full-potential linearized augmented plane wave (FP-LAPW) method [22, 23] based on density functional theory (DFT), as implemented in the WIEN2k code [24]. In these calculations, the exchange–correlation functional was approximated using the generalized gradient approximation (GGA) in the Perdew–Burke–Ernzerhof (GGA-PBE) [25, 26] formulation. In the FP-LAPW method, the crystal unit cell is divided into two distinct regions, i.e., the non-overlapping atomic spheres, called muffin-tin (MT) spheres, and the interstitial region (IR) outside these spheres. Accordingly, two different sets of basis functions are used, i.e., the plane wave (PW) expansion in the interstitial region and the spherical harmonics basis functions inside the muffin-tin spheres, with the angular momentum quantum number extended up to $l_{\max} = 10$. The core and valence states are treated differently. The core states are treated relativistically, while valence states are treated within a scalar relativistic approximation. The muffin-tin radii R_{MT} are chosen such that the spheres do not overlap. The plane wave cutoff is defined by the parameter $R_{\mathrm{MT}}\,K_{\max} = 7$, where $K_{\max}$ is the largest reciprocal lattice vector used in the plane wave expansion. The cutoff for the Fourier expansion of the charge density is set to $G_{\max} = 12$ (a.u.)$^{-1}$.

To ensure total energy convergence, the number of k-points was varied until the cutoff energy convergence criterion of 10^{-4} Ry was satisfied. Finally, the lattice constant and bulk modulus were determined by fitting the total energy as a function of volume using the Birch–Murnaghan equation of state.

3. Results and discussion

3.1. Structural properties

We begin by examining the structural properties, as this step is essential for assessing the stability of $TlSrF_3$ and serves as a foundation for evaluating its other physical characteristics. $TlSrF_3$ crystallizes in a cubic perovskite structure, crystallizing in the P$m-3m$ (no. 221) space group. In this structure, the strontium (Sr) cation occupies the Wyckoff position (0, 0, 0), located at the corners of the cubic unit cell, while the thallium (Tl) cation is situated at the body center, corresponding to the Wyckoff position ($\frac{1}{2}$, $\frac{1}{2}$, $\frac{1}{2}$). The fluorine (F) anions reside at the face centers of the cube, occupying the Wyckoff positions ($\frac{1}{2}$, 0, 0), (0, $\frac{1}{2}$, 0), and (0, 0, $\frac{1}{2}$), or equivalently, (0, $\frac{1}{2}$, $\frac{1}{2}$), ($\frac{1}{2}$, 0, $\frac{1}{2}$), and ($\frac{1}{2}$, $\frac{1}{2}$, 0), depending on the chosen convention of origin [27, 28]. This atomic arrangement is characteristic of cubic fluoro-perovskites. The crystal structure is illustrated in Fig. 1.

The investigation starts with the calculation of the total energy as a function of volume, which is subsequently fitted using the Birch–Murnaghan equation of state [29]. The resulting energy–volume curve is shown in Fig. 2. From this fitting, key

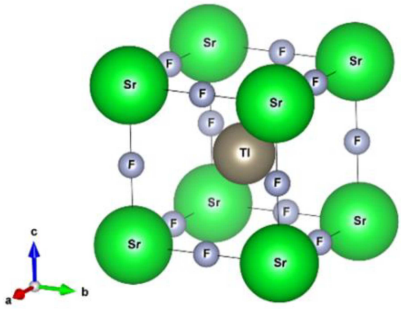

Fig. 1. Crystal structure of cubic perovskite $TlSrF_3$.

TABLE I

Calculated lattice constant (a_0 [Å]), bulk modulus (B [GPa]), pressure derivative of the bulk modulus (B' [GPa]), energy (E [Ry]), ground state volume (V_0 [(a.u.)^3)], bond lengths (d [Å]), and tolerance factor (t) of cubic $TlSrF_3$.

Parameter	Present results	Other results
a_0 [Å]	4.7928	4.8879 [18], 4.790 [30], 4.78 [17], 4.724 [31]
B [GPa]	41.0973	36.45 [18], 40.70 [30]
B' [GPa]	5.0574	5.0592 [18], 5.0 [30]
E [Ry]	−47536.7906	–
V_0 [(a.u.)^3]	742.9521	788.0924 [18], 741.523 [30]
$\langle d_{\mathrm{Tl-F}} \rangle$ [Å]	6.4043	–
$\langle d_{\mathrm{Sr-F}} \rangle$ [Å]	4.5285	–
$\langle d_{\mathrm{Tl-Sr}} \rangle$ [Å]	7.8436	–
t	0.9998	–

structural parameters of the compound including the equilibrium lattice constant (a_0), bulk modulus (B), its pressure derivative (B'), ground-state volume (V_0), and the total energy (E), were extracted and are summarized in Table I.

Table I presents the ground state properties of cubic $TlSrF_3$. The optimized lattice parameter was found to be 4.7928 Å. Comparison with previous studies reveals that our result is consistent with the values reported in [17] and [30], validating the accuracy of the exchange–correlation potential used in this work. The slight deviations observed compared to the papers [18] (4.8879 Å) and [31] (4.724 Å) may be attributed to differences in the computational methods or pseudo-potentials used in those studies. Our bulk modulus $B = 41.10$ GPa is in excellent agreement with the literature value 40.70 GPa [30] ($\sim 1\%$) and higher than the value 36.45 GPa reported in [18] ($\sim 12.7\%$). Our pressure derivative $B' \approx 5.06$ is essentially identical to the previous results (5.0 [18] and 5.052 [30]), indicating a robust description of the compression behavior

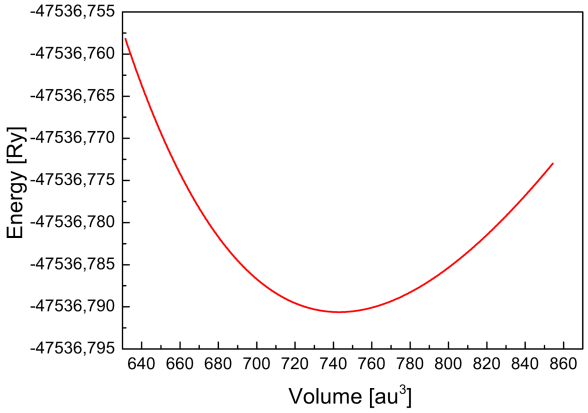

Fig. 2. Energy as a function of volume for cubic unit cell of $TlSrF_3$.

across independent studies. Additionally, the geometric stability of the crystal was assessed using the Goldschmidt tolerance factor (t). The calculated value of $t = 0.9998$ indicates that the $TlSrF_3$ compound retains ideal cubic symmetry without significant distortion.

The bond lengths of Tl–F, Sr–F, and Tl–Sr were also calculated, as these are critical for assessing the structural stability of perovskite compounds. Additionally, the Goldschmidt tolerance factor (t) was computed using the average bond lengths (here denoted with $\langle d \rangle$) of Tl–F and Sr–F, according to the following relation [32]

$$t = \frac{0.707\,\langle d_{\mathrm{Tl-F}} \rangle}{\langle d_{\mathrm{Sr-F}} \rangle}. \quad (1)$$

The obtained value of t falls within the characteristic range of cubic perovskite phases (0.95–1.04) [32], supporting the argument for the structural stability of $TlSrF_3$. To the best of our knowledge, no experimental data on the bulk modulus of this compound has been reported to date. However, the calculated lattice parameter shows good agreement with previous theoretical predictions, as evident in Table I.

3.2. Electronic structure and density of states (DOS)

To explore the electronic properties of $TlSrF_3$ and gain insights into its fundamental physical characteristics, we calculated the electronic band structure, along with the total and partial densities of states (DOS). These calculations provide key information for determining whether the compound behaves as an insulator, semiconductor, or metal.

The band structure was computed along high-symmetry directions in the first Brillouin zone, specifically: Γ (0, 0, 0), X ($\frac{1}{2}$, 0, 0), M ($\frac{1}{2}$, $\frac{1}{2}$, 0), and R ($\frac{1}{2}$, $\frac{1}{2}$, $\frac{1}{2}$), in the energy range from −4 to 12 eV at zero pressure. The Fermi level E_{F} is set

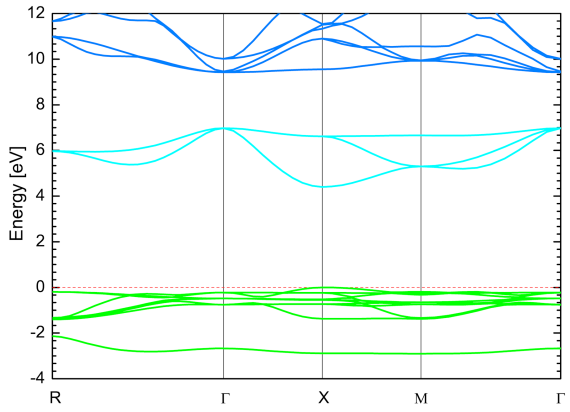

Fig. 3. Calculated band structures of the cubic perovskite $TlSrF_3$ using the PBE-GGA potential.

as the zero-energy reference. The calculated band structure is presented in Fig. 3. As shown, both the valence band maximum (VBM) and conduction band minimum (CBM) occur at the X-point of the Brillouin zone, indicating that $TlSrF_3$ is a direct band gap insulator with an estimated gap of approximately 4.40 eV.

The computed band gap values at various high-symmetry points are summarized in Table II. Although no experimental band gap values are currently available for this compound, these theoretical predictions serve as a useful benchmark for future experimental and computational studies.

In the present work, the band gaps were found to be 7.20, 4.40, 5.49, and 6.16 eV along the Γ–Γ, X–X, M–M, and R–R directions, respectively. Our value calculated at the point X (4.40 eV) shows excellent agreement with the previous GGA calculations (4.37 eV) reported in [17]. However, our result remains lower than the values obtained via the hybrid Heyd–Scuseria–Ernzerhof (HSE) functional (i.e., 5.74 eV [17]) or Tran–Blaha modified Becke–Johnson (TB-mBJ) potential (i.e., 6.03 eV [18]) — these discrepancies can be attributed to the underestimation of band gaps within standard DFT.

Subsequently, the total and partial densities of states (DOS) were computed and are shown in Fig. 4. The total DOS reveals the electronic structure of $TlSrF_3$, with the Fermi level (E_F) set to 0 eV. The valence band maximum (VBM) lies just below E_F and is dominated by contributions from F-p orbitals, exhibiting a single peak located within the range of approximately −2 to −6 eV. This behavior is consistent with typical perovskite halides, where anion-p states form the top of the valence band. Deeper valence states (from −6 to −12 eV) arise primarily from Tl-p states, with additional contributions from F-p orbitals.

The conduction band minimum (CBM), located $\simeq$ 1–4 eV above E_F, is characterized by strong hybridization between the Tl and Sr total states, indicating metal–cation driven dispersive bands.

TABLE II

Electronic band gap values [in eV] at selected high-symmetry points in the Brillouin zone of $TlSrF_3$.

Compound $TlSrF_3$				
$E_g^{\Gamma-\Gamma}$	E_g^{X-X}	E_g^{M-M}	E_g^{R-R}	Ref.
7.20	4.40	5.49	6.16	Present work
–	4.37 (GGA)	–	–	[17]
–	5.74 (HSE)	–	–	[17]
–	6.03 (TB-mBJ)	–	–	[18]

Sr-p orbital contributes moderately near E_F, while the contribution of F total states remains low in the conduction region, which underscores the ionic–covalent character.

3.3. Optical properties

Examining the optical properties of $TlSrF_3$ is vital for understanding its response to electromagnetic radiation and for determining its potential for applications in optoelectronic devices. Optical parameters were computed using the FP-LAPW method with the GGA-PBE approximation, in the photon energy range of 0–14 eV.

The frequency-dependent complex dielectric function $\varepsilon(\omega)$ serves as a basis for determining several optical quantities. These quantities include the real and imaginary parts of the dielectric function ($\varepsilon_1(\omega)$ and $\varepsilon_2(\omega)$, respectively), the refractive index $n(\omega)$, the extinction coefficient $k(\omega)$, the absorption coefficient $I(\omega)$, the reflectivity $R(\omega)$, the optical conductivity $\sigma(\omega)$, and the electron energy loss function $L(\omega)$. They are defined by the following relations

$$\varepsilon(\omega) = \varepsilon_1(\omega) + \mathrm{i}\varepsilon_2(\omega), \tag{2}$$

$$n(\omega) = \sqrt{\frac{\varepsilon_1(\omega)}{2} + \frac{\sqrt{\varepsilon_1^2(\omega) + \varepsilon_2^2(\omega)}}{2}}, \tag{3}$$

$$k(\omega) = \sqrt{-\frac{\varepsilon_1(\omega)}{2} + \frac{\sqrt{\varepsilon_1^2(\omega) + \varepsilon_2^2(\omega)}}{2}}, \tag{4}$$

$$I(\omega) = \frac{2\omega\, k(\omega)}{c}, \tag{5}$$

$$R(w) = \frac{(1-n)^2 + k^2}{(1+n)^2 + k^2}, \tag{6}$$

$$\sigma(\omega) = \frac{2\, W_{ev}\, \hbar\, \omega}{E_0} = \frac{\omega}{4\pi}\, \varepsilon_2(\omega), \tag{7}$$

$$L(\omega) = -\frac{\varepsilon_2(\omega)}{\varepsilon_1^2(\omega) + \varepsilon_2^2(\omega)}, \tag{8}$$

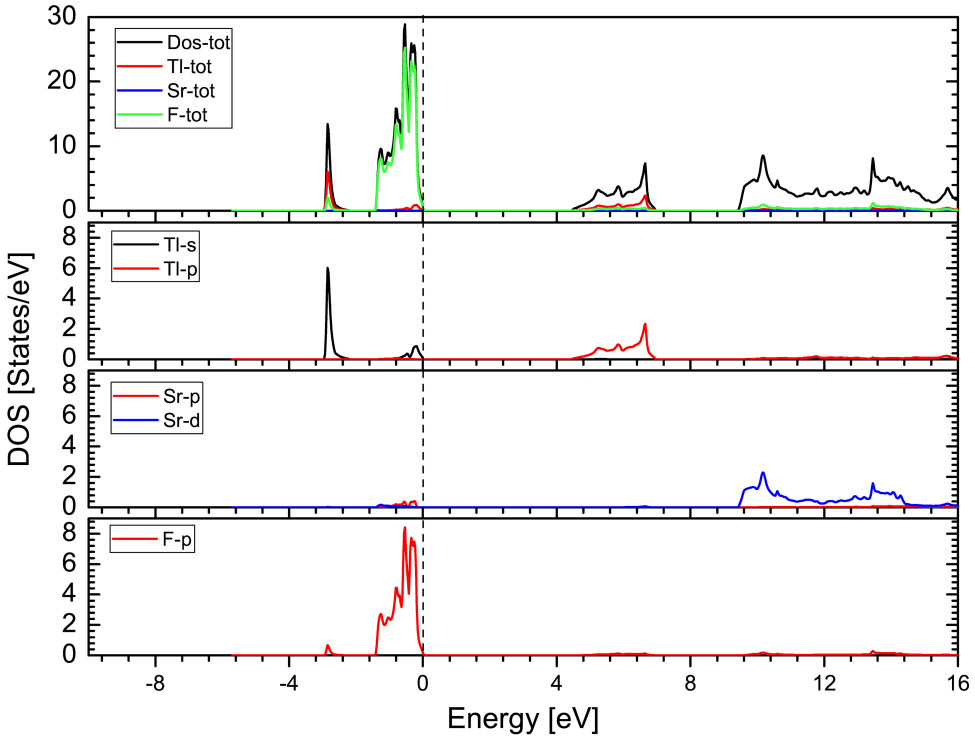

Fig. 4. Total and partial densities of states of the cubic perovskite $TlSrF_3$.

where ω is the angular frequency, $\hbar$ is the reduced Planck constant, W_{ev} is the parameter describing interband electronic transitions, and E_0 is the external electric field amplitude.

3.3.1. Dielectric function

In the present study, the dielectric function for perovskite $TlSrF_3$ was computed to elucidate the material's optical response. The complex dielectric function consists of the real and imaginary parts, $\varepsilon_1(\omega)$ and $\varepsilon_2(\omega)$, respectively, as defined in (2). The calculated spectra for $\varepsilon_1(\omega)$ and $\varepsilon_2(\omega)$ in the photon energy range 0–14 eV are illustrated in Fig. 5a and b, respectively.

At zero photon energy, the static dielectric constant was found to be $\varepsilon_1(0) \approx 2.3$. A prominent peak in the $\varepsilon_1(\omega)$ function appears near 5.0 eV in the UV region, corresponding to a strong interband transition. This feature indicates the presence of dense electronic states, likely resulting from orbital hybridization. Beyond this peak, $\varepsilon_1(\omega)$ decreases sharply and displays several oscillations, attributed to complex interband effects.

The static dielectric tensor shows near-perfect isotropy, as evidenced by $\varepsilon_{xx}(0) = \varepsilon_{zz}(0) = 2.30$ and $n_{xx}(0) = n_{zz}(0) = 1.52$ (differences < 0.01; see Table III). Overall, the computed frequency-dependent spectra display a high degree of isotropy between the $\varepsilon_{xx}(\omega)$ and $\varepsilon_{zz}(\omega)$ components, in line with the cubic symmetry of $TlSrF_3$. This behavior corroborates the structural analysis and highlights the compound's promise for isotropic optical and photonic devices.

TABLE III

Static dielectric constants and refractive indices.

Component	$\varepsilon_1(0)$	$n(0)$
Along xx	2.30	1.52
Along zz	2.30	1.52
Difference	< 0.01	< 0.01

The spectrum of $\varepsilon_2(\omega)$ shows that absorption starts abruptly at ≈ 4.2 eV. Below this energy, $\varepsilon_2(\omega)$ remains near zero, confirming that $TlSrF_3$ is highly transparent in the visible region (1.65–3.1 eV). A pronounced peak is observed at 5.6 eV, followed by successive peaks at 6.7, 8.1, 9.4, and 10.4 eV. These are attributed to allowed interband transitions. Above 10.4 eV, $\varepsilon_2(\omega)$ gradually decreases, with minor fluctuations likely arising from high-energy interband transitions involving deep valence states or core-level excitations.

3.3.2. Refractive index and extinction coefficient

The refractive index $n(\omega)$ and the extinction coefficient $k(\omega)$ are key optical parameters that characterize the interaction of electromagnetic

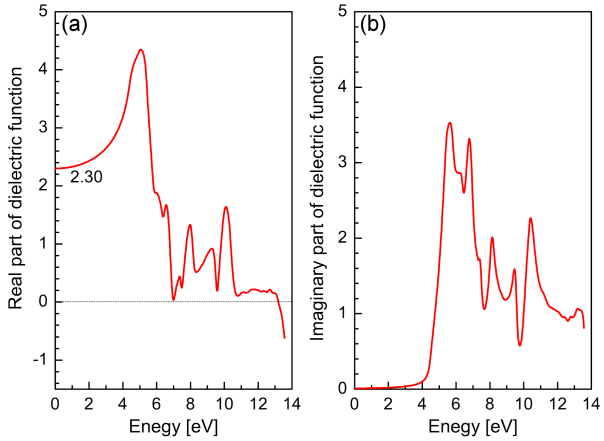

Fig. 5. Computed (a) real and (b) imaginary parts of the dielectric function for the cubic perovskite $TlSrF_3$.

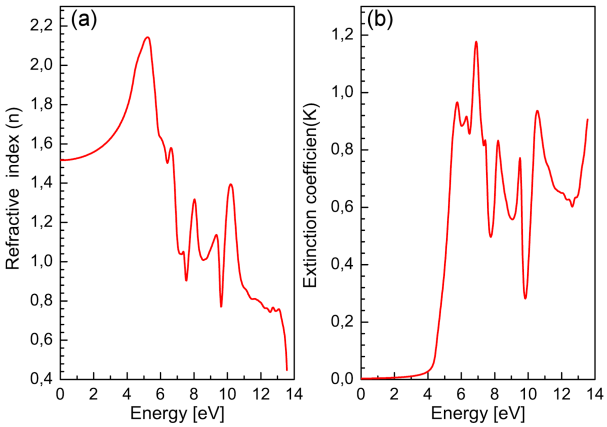

Fig. 6. Extinction coefficient and refractive index computed for the cubic perovskite $TlSrF_3$.

radiation with materials. The refractive index $n(\omega)$, representing the real part of the complex refractive index, describes the phase velocity of light in the absence of absorption. Conversely, the extinction coefficient $k(\omega)$, which is the imaginary part, quantifies the material's ability to absorb incident light. The calculated spectra of both quantities are illustrated in Fig. 6.

At zero photon energy, the static refractive index is found to be $n(0) \approx 1.5$, indicating high optical transparency in the visible region. The maximum refractive index of ≈ 2.1 is observed at around 5.2 eV, corresponding to enhanced optical activity in the UV domain. Beyond this peak, $n(\omega)$ gradually decreases, with minor oscillations attributed to variations in the density of states and interband transitions.

The extinction coefficient $k(\omega)$ remains nearly zero in the range 0–4 eV, confirming negligible absorption in the visible spectrum. A sharp onset of absorption is evident at ≈ 4.2 eV, followed by multiple pronounced peaks near 5.7, 6.3, 8.8, and 10.5 eV.

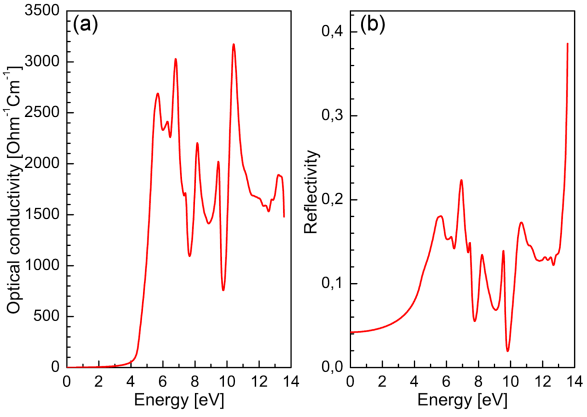

Fig. 7. Optical conductivity and reflectivity computed for the cubic perovskite $TlSrF_3$.

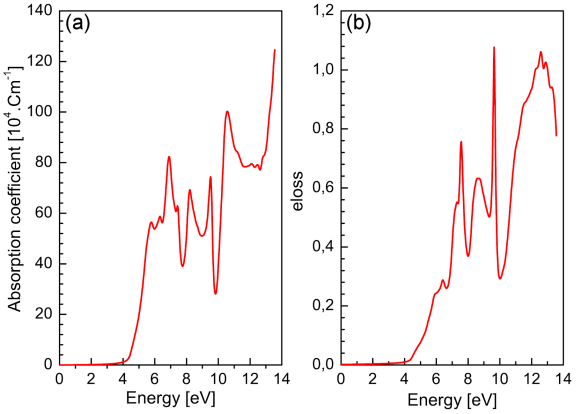

Fig. 8. Absorption coefficient and energy loss function computed for the cubic perovskite $TlSrF_3$.

These features arise from interband transitions from occupied valence states to unoccupied conduction bands, consistent with the observed dielectric function spectra.

3.3.3. Optical conductivity and reflectivity

Figure 7 presents the calculated optical conductivity $\sigma(\omega)$ and reflectivity $R(\omega)$ spectra of $TlSrF_3$. The critical point for optical conduction in the $\sigma(\omega)$ spectrum is identified at $\approx$ 4.2 eV, signaling the onset of notable interband electronic transitions. A sharp rise in conductivity above this threshold reflects increased electronic excitation in the band gap. The intensity and sharpness of the conductivity peaks are strongly influenced by the density of occupied and unoccupied states, as well as the degeneracy of the involved energy levels [33].

Several prominent peaks in the $\sigma(\omega)$ spectrum appear near 5.6, 6.8, 8.1, and 10.4 eV, with the maximum optical conductivity reaching ≈ 3180 $(\Omega\ \mathrm{cm})^{-1}$. These features are in strong

agreement with the peaks observed in the dielectric and absorption spectra, thereby validating the proposed interband transition mechanisms.

The static reflectivity $R(0)$ is calculated to be $\approx 4.2\%$. In the low-energy region (0–3.5 eV), $R(\omega)$ remains below 10%, indicating excellent transparency in the visible range, an essential requirement for applications in optoelectronic and scintillation detectors. Beyond this range, the reflectivity increases nonlinearly, peaking at about 22.4% near 6.9 eV, suggesting effective reflective behavior in the UV domain.

3.3.4. Absorption coefficient and energy loss function

The absorption coefficient $I(\omega)$ and the electron energy loss function $L(\omega)$ of $TlSrF_3$ are illustrated in Fig. 8.

The onset of significant optical absorption is observed at ≈ 4.2 eV, marking the beginning of prominent interband electronic transitions. A steep increase in $I(\omega)$ occurs between 5.7 and 10.5 eV, indicating strong photon absorption in the ultraviolet region. The absorption coefficient reaches a peak value of $\approx 100.5 \times 10^4$ cm^{-1} at 10.5 eV, reflecting the material's high efficiency in absorbing UV radiation.

The energy loss function $L(\omega)$, which describes the energy dissipated by fast electrons passing through the material, exhibits two pronounced peaks at around 9.6 and 12.5 eV. These peaks are attributed to bulk plasmon resonances, indicative of collective oscillations of the electron cloud. The appearance of these features corroborates the interband transitions observed in other optical spectra and underscores the potential of $TlSrF_3$ for applications involving high-energy photon interactions.

3.4. Thermodynamic properties

The thermodynamic behavior of the cubic perovskite $TlSrF_3$ under varying temperature and pressure conditions was investigated using the quasi-harmonic Debye model, as implemented in the GIBBS2 code [34, 35] in conjunction with *ab initio* calculations. The analysis was carried out over a temperature range of 0–1000 K and a pressure range of 0–35 GPa, focusing on several key thermodynamic quantities: bulk modulus (B), equilibrium volume (V), isobaric heat capacity (C_p), isochoric heat capacity (C_v), Debye temperature (θ_D), entropy (S), thermal expansion coefficient (α), and Gibbs free energy (G).

The temperature dependence of these properties at various pressures is depicted in Figs. 9–12. As shown in Fig. 9, the equilibrium volume V increases monotonically with temperature at constant pressure, consistent with thermal expansion behavior.

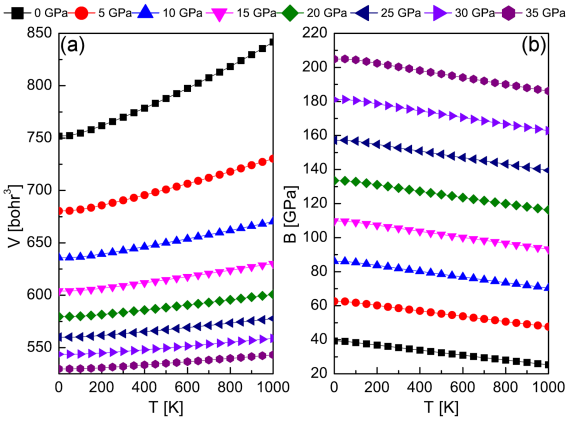

Fig. 9. Variation of (a) volume V and (b) bulk modulus B with temperature of cubic perovskite $TlSrF_3$.

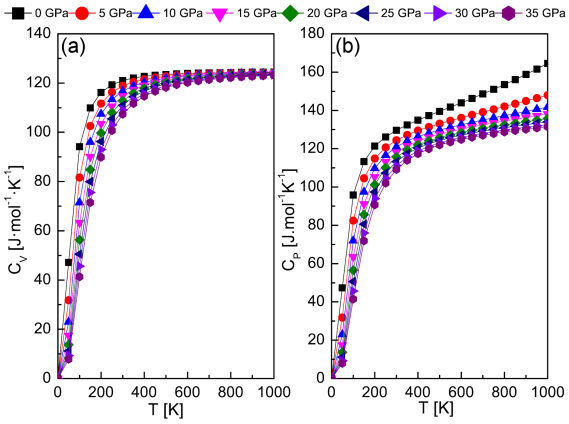

Fig. 10. Variation of (a) isochoric heat capacity C_v and (b) isobaric heat capacity C_p with temperature of cubic perovskite $TlSrF_3$.

In contrast, the bulk modulus B decreases with increasing temperature, indicating softening of the lattice. However, as pressure increases, B increases significantly, reflecting enhanced resistance to volume changes and increased lattice stiffness.

Figure 10 shows that both the isochoric and isobaric heat capacities (C_v and C_p, respectively) increase monotonically with temperature and approach the Dulong–Petit limit at high temperatures, which is characteristic of crystalline solids. A slight reduction in both quantities is observed under elevated pressures, suggesting a subtle stiffening of phonon modes due to compression.

As illustrated by the results in Figs. 9 and 10, the observed decrease in bulk modulus with increasing temperature is directly attributed to lattice softening, which facilitates atomic vibrations and enhances both C_v and C_p. Conversely, the increase in B under higher pressure corresponds to stronger interatomic bonding, resulting in reduced vibrational amplitudes and slightly lower heat capacities.

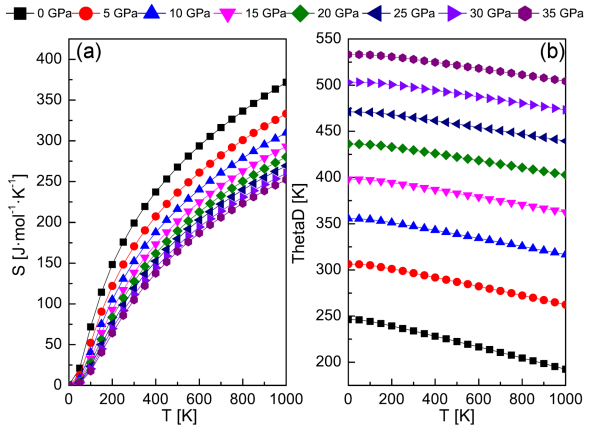

Fig. 11. Variation of (a) entropy S and (b) Debye temperature θ_D with temperature of cubic perovskite $TlSrF_3$.

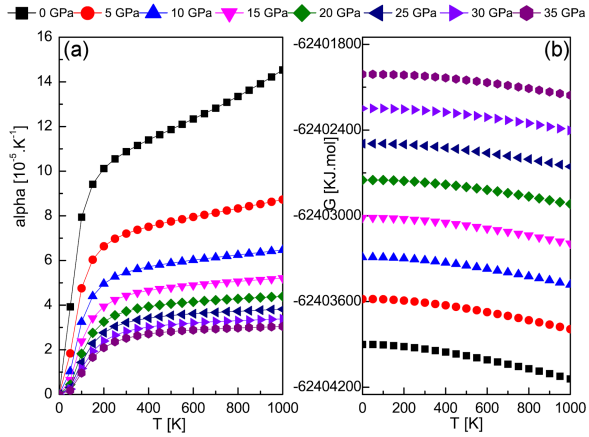

Fig. 12. Variation of (a) thermal expansion coefficient α and (b) Gibbs free energy G with temperature of cubic perovskite $TlSrF_3$.

This correlation highlights the intrinsic coupling between elastic and thermodynamic properties, confirming that variations in temperature and pressure simultaneously influence the material's mechanical rigidity and vibrational behavior.

Figure 11 shows that the entropy S steadily increases with temperature, reflecting enhanced vibrational activity and configurational disorder. Conversely, the entropy decreases with applied pressure, which can be attributed to the suppression of crystal lattice vibrations caused by unit cell compression. The Debye temperature θ_D, which provides insight into lattice dynamics and bonding strength, increases markedly with pressure, indicating stronger interatomic interactions in the compressed state.

As illustrated in Fig. 12, the thermal expansion coefficient α decreases with increasing pressure, suggesting good structural resistance to thermal deformation — an essential characteristic for high-temperature applications.

Furthermore, throughout the investigated temperature and pressure ranges, the Gibbs free energy G remains negative, with its magnitude decreasing as temperature increases. This trend confirms the thermodynamic stability of $TlSrF_3$ under the studied conditions. Overall, this compound exhibits notable thermal and mechanical robustness.

4. Conclusions

In this work, the structural, electronic, optical, and thermodynamic properties of the fluoroperovskite $TlSrF_3$ were systematically investigated using first-principles calculations within the FP-LAPW method and the GGA-PBE approximation. Optimized structural parameters confirm the stability of the cubic perovskite phase ($Pm{-}3m$), which was supported by the calculated tolerance factor and the equilibrium energy–volume relation. Analysis of the electronic band-structure reveals a direct, wide band gap ($\sim$ 4.4 eV at the X–X transition), classifying $TlSrF_3$ as an insulating material with potential for ultraviolet-active applications.

Optical analysis shows strong UV absorption, high transparency in the visible region, and pronounced optical isotropy, consistent with cubic symmetry. These properties underscore the material's suitability for optoelectronic and scintillation-based detection technologies. Furthermore, thermodynamic modeling using the quasi-harmonic Debye approach indicates that $TlSrF_3$ maintains mechanical and thermal stability over wide ranges of temperature and pressure. This also agrees with the trends in heat capacity and bulk modulus, reflecting the coupling between elastic stiffness and lattice vibrations.

Overall, the predicted combination of structural robustness, optical transparency, and thermal stability identifies $TlSrF_3$ as a promising candidate for radiation detection, UV-optical components, and related energy-conversion applications. Future work should include experimental validation and Monte Carlo radiation-transport simulations to quantify its scintillation performance — particularly light yield and energy resolution — in practical device configurations.

References

[1] A.A. Yahaya, W.A. Yahya, A.S. Ahmed, A.A. Sholagberu, *Acta Phys. Pol. A* **145**, 194 (2024).

[2] Z. Ali, I. Ahmad, I. Khan, B. Amin, *Intermetallics* **31**, 287 (2012).

[3] F. Hamioud, G.S. AlGhamdi, S. Al-Omari, A.A. Mubarak, *Int. J. Mod. Phys. B* **30**, 1650031 (2016).

[4] X. Li Y. Dan, R. Dong, Z. Cao, C. Niu, Y. Song, S. Li, J. Hu, *Appl. Sci.* **9**, 5510 (2019).

[5] L. Benahmedi, A. Besbes, R. Djelti, *Acta Phys. Pol. A* **147**, 393 (2025).

[6] P. Long, D. Pang, X. Liu, Z. Yi, *J. Am. Ceram. Soc.* **102**, 1741 (2019).

[7] P. Pitriana, T.D.K. Wungu, H. Herman, R. Hidayat, *Results Phys.* **15**, 102592 (2019).

[8] A. Stoddart, *Nat. Rev. Mater.* **3**, 226 (2018).

[9] D. Li, J. Shi, Y. Xu, Y. Luo, H. Wu, Q. Meng, *Natl. Sci. Rev.* **5**, 559 (2018).

[10] P. Sharma, P. Ranjan, T. Chakraborty, *Chem. Phys. Impact* **7**, 100344 (2023).

[11] Abdullah, M. Sajjad, U.A. Khan, H. Ullah, A. Alhodaib, M. Amami, V. Tirth, A. Zaman, Shaziab, *RSC Adv.* **12**, 27508 (2022).

[12] A.A. Mousa, *Int. J. Mod. Phys. B* **28**, 1450139 (2014).

[13] S.C. Mouna, M. Radjai, M.A. Rahman, A. Bouhemadou, Abdullah, D. Houatis, D. Allali, S.S. Essaoud, H. Allaf, *J. Phys. Condens. Matter* **36**, 055701 (2024).

[14] D. Sirbu, H.C.L. Tsui, N. Alsaif, S. Iglesias-Porras, Y. Zhang, M. Wang, M. Liu, A.C. Peacock, P. Docampo, N. Healy, *ACS Photon.* **8**, 2450 (2021).

[15] M.Z. Tun, P. Pansa-Ngat, P. Ruankham et al., *Sci. Rep.* **13**, 2965 (2023).

[16] M. Sohail, M. Husain, N. Rahman et al., *RSC Adv.* **12**, 7002 (2022).

[17] S. Khan, A. Gassoumi, A.U. Rahman, F. Ullah, R. Ahmad, N. Mehmood, M. Abdul, A.H. Shah, *Phys. Scr.* **98**, 055907 (2023).

[18] G. Ayub, A. Rauf, M. Husain et al., *ACS Omega* **8**, 17779 (2023).

[19] X. Wu, A. Li, M. Yang, X. Hao, L. Wu, R. Su, J. Zhang, *J. Mater. Chem. C* **12**, 8647 (2024).

[20] M. Zaman, M.A. Rehman, I. Zeba, M. Shakil, S.S.A. Gillani, *Comput. Condens. Matter* **44**, e01075 (2025).

[21] J. ur Rehman, M. Usman, M.B. Tahir, A. Hussain, M.A. Rehman, N. Ahmad, H. Alrobei, K. Shahzad, A.M. Ali, S. Muhammad, *Solid State Commun.* **334–335**, 114396 (2021).

[22] P. Blaha, K. Schwarz, P. Sorantin, S.B. Trickey, *Comput. Phys. Commun.* **59**, 399 (1990).

[23] G.K.H. Madsen, P. Blaha, K. Schwarz, E. Sjöstedt, L. Nordström, *Phys. Rev. B* **64**, 195134 (2001).

[24] P. Hohenberg, W. Kohn, *Phys. Rev.* **136**, B864 (1964).

[25] P. Blaha, K. Schwarz, G.K.H. Madsen, D. Kvasnicka, J. Luitz, "WIEN2k: An Augmented Plane Wave + Local Orbitals Program for Calculating Crystal Properties", Technische Universität Wien, Wien 2001.

[26] J.P. Perdew, K. Burke, M. Ernzerhof, *Phys. Rev. Lett.* **77**, 3865 (1996).

[27] J.E. Saal, S. Kirklin, M. Aykol, B. Meredig, C. Wolverton, *JOM* **65**, 1501 (2013).

[28] S. Kirklin, J.E. Saal, B. Meredig, A. Thompson, J.W. Doak, M. Aykol, S. Rühl C. Wolverton, *npj Comput. Mater.* **1**, 15010 (2015).

[29] F. Birch, *Phys. Rev.* **71**, 809 (1947).

[30] K. Murad, M. Noman, S. Khan, R. Neffati, M.W. Ashraf, G. Murtaza, *Phys. Scr.* **98**, 075945 (2023).

[31] J.I. Gómez-Peralta, X. Bokhimi, *J. Solid State Chem.* **285**, 121253 (2020).

[32] N. Xu, H. Zhao, X. Zhou, W. Wei, X. Lu, W. Ding, F. Li, *Int. J. Hydrogen Energy* **35**, 7295 (2010).

[33] M. Choi, F. Oba, I. Tanaka, *Appl. Phys. Lett.* **98**, 172901 (2011).

[34] A. Otero-de-la-Roza, V. Luaña, *Comput. Phys. Commun.* **182**, 1708 (2011).

[35] J.A. Abraham, *Int. J. Mod. Phys. B* **33**, 1950314 (2019).